Nanoscale

COMMUNICATION

View Article Online
View Journal

Cite this: DOI: 10.1039/d6nr00764c

Received 24th February 2026,
Accepted 11th April 2026

DOI: 10.1039/d6nr00764c

rsc.li/nanoscale

Ultra-sensitive mercury sensor based on thin film transistor using flavin self-assembly on monochiral carbon nanotubes

Dong Hwan Kim, [a] Seongjoo Hwang, [b] Yoonbeen Kang [b] and Sang-Yong Ju *[a,b]

Achieving ultra-sensitive mercury detection requires precise molecular design and seamless integration with electronic sensing systems. Here, we show that a monochiral single-walled carbon nanotube (SWCNT) thin-film transistor (TFT) sensor, helically wrapped with flavin molecules, achieves remarkable sensitivity to mercury ions down to 1 pM. To accomplish this, we adopted several complementary strategies. Monochiral SWCNTs were first isolated using *N*-dodecyl flavin (FC12) in a mixed solvent system, ensuring high structural uniformity. The resulting FC12-sorted SWCNT complexes were then efficiently assembled onto TFT devices through mixed self-assembled monolayers, maximizing device sensitivity. In addition, a distinctive coordination-based sensing motif, combined with PEGylation of the gold electrodes, suppressed nonspecific interactions and enhanced selectivity. The finalized molecular recognition-driven TFT sensor detects mercury ions through the formation of a flavin–Hg–flavin coordination triad across a concentration range of 1–100 pM, a response not observed with other metal ions. By tightly integrating molecular recognition with electronic transduction, this platform enables highly precise and ultra-sensitive detection, offering strong potential for early identification of environmental contaminants and disease-associated biomarkers.

Introduction

Mercury ions (Hg^{2+}) continue to pose a serious global environmental and public health threat because of their persistence in ecosystems, tendency to bioaccumulate, and pronounced neurotoxicity even at extremely low concentrations.[1,2] Human activities—including mining operations, fossil fuel combustion, and improper waste management—have substantially increased mercury concentrations in both aquatic and terrestrial environments. This escalation underscores the urgent need for highly sensitive, selective, and portable detection systems suitable for on-site monitoring. For example, the World Health Organization (WHO) and other regulatory agencies have established permissible limits for toxic metal ions in water: iron, zinc, and copper are regulated at levels of approximately 1–10 ppm (1 ppb = ~5.0×10^{-8} M), whereas more toxic metals such as cadmium, lead, arsenic, chromium, and mercury are restricted to much lower concentrations in the range of 1–10 ppb.[3,4]

Traditional analytical methods for mercury detection—such as atomic absorption spectroscopy, inductively coupled plasma mass spectrometry, and cold vapor analysis—provide excellent accuracy and sensitivity. However, their reliance on costly instrumentation, extensive sample preparation procedures, and well-equipped laboratory facilities limits their practicality for field deployment. Consequently, there has been growing interest in the development of affordable, compact, and real-time electronic sensing technologies capable of reliable operation under on-site conditions.

Thin-film transistors (TFTs) incorporating nanomaterials have emerged as highly effective transduction platforms for chemical and biological sensing applications.[5–11] Among these materials, single-walled carbon nanotube (SWCNT) networks have received considerable attention owing to their outstanding electrical conductivity, large surface-to-volume ratio, chemical robustness, and compatibility with flexible substrates.[12–16] Nevertheless, as-synthesized SWCNTs typically consist of a heterogeneous mixture of metallic and semiconducting (*s*-) nanotubes, leading to device-to-device variability and diminished sensing reliability. The implementation of monochiral *s*-SWCNTs offers a promising solution to this challenge by delivering uniform electronic properties, enhanced reproducibility, and improved sensitivity in transistor-based sensing platforms.[17,18]

In addition to the electronic channel material, the sensing performance of TFT devices is strongly influenced by the interfacial chemistry between the analyte and the semiconducting layer.[19] Molecular self-assembly provides an effective strategy for constructing well-ordered and chemically selective interfaces without compromising the intrinsic electronic character-

[a]Graduate School of Convergence Semiconductor Collaboration Process, Yonsei University, Seoul 03722, Republic of Korea. E-mail: syju@yonsei.ac.kr
[b]Department of Chemistry, Yonsei University, Seoul 03722, Republic of Korea

istics of SWCNTs.[20] Flavin molecules, derived from riboflavin (vitamin B_2), exhibit strong π–π interactions with SWCNT sidewalls[21,22] and contain redox-active isoalloxazine moieties capable of coordinating metal ions.[23] This dual functionality enables flavins to establish stable supramolecular assemblies on SWCNT surfaces while simultaneously serving as selective binding sites for heavy metal ions such as Hg^{2+}. Importantly, the noncovalent nature of these interactions preserves charge transport within the SWCNT channel while introducing specific chemical recognition capabilities.

Recent investigations have shown that flavin-functionalized nanostructures can display selective responses toward metal ions, driven by charge-transfer interactions and dipole modulation effects associated with metal–ligand coordination.[23] When incorporated into a TFT configuration,[24] these interfacial processes directly influence key device parameters—including channel conductance, threshold voltage, and carrier mobility—thereby enabling label-free and real-time electrical detection. Furthermore, the controlled self-assembly of flavin molecules on monochiral semiconducting SWCNTs is anticipated to generate a homogeneous sensing interface, improving signal uniformity and device-to-device reproducibility relative to randomly functionalized counterparts.

In this work, we report the development of an ultrasensitive mercury-recognition TFT platform based on a random network of monochiral *s*-SWCNTs noncovalently wrapped with *N*-dodecyl flavin (FC12). A precisely engineered transistor architecture was designed to suppress nonspecific interactions while facilitating FC12-mediated molecular recognition at the SWCNT surface. This molecular-level interfacial design enabled stable transistor operation in liquid-phase environments. Consequently, the device demonstrates selective mercury detection through the formation of a flavin–Hg–flavin coordination complex, which induces significant modulation of the electrical transport properties of the FC12/monochiral SWCNT TFT.

Experimental

Materials and instrumentation

FC12 was synthesized according to the literature.[25] SWCNT prepared by high-pressure carbon monoxide (HiPco) method[26] was purchased from NanoIntegris Inc. (raw grade (minimum SWCNT contents >65%), batch #: HR29-073). Chloro(dimethyl) ethylsilane, chloro (dimethyl)octylsilane, poly(ethylene glycol) (PEG) methyl ether thiol (average molecular weight (M.W.) = 800 Da), $HgCl_2$, and $FeCl_3$ were purchased from Merck. Nickel chloride hexahydrate ($NiCl_2{\cdot}6H_2O$) was purchased from Samchun chemicals. Chloroform (Ch) and toluene (Tol) solvents were reagent grade and dried over 3 Å molecular sieves (Alfa Aesar) for a day before dispersion. The as-received Si wafer (285 nm thick SiO_2/Si substrate, ShinEtsu) was cut into pieces with a 1 × 1 cm^2 size, and further rinsed with methanol, acetone, and isopropanol, and was subjected to drying with an N_2 stream. All the measurements were carried out at room temperature unless otherwise noted. The absorption measurements were conducted using a V-770 (JASCO) with two-beam geometry. Absorption cuvettes with a 10 mm path length (QS grade, Hellma) were used. Atomic force microscopy (AFM) measurements were performed using an NX10 (Park Systems). Fluorescence measurements were performed using a spectrofluorometer (Jobin–Yvon Spex Fluorolog 3-211, Horiba), having a Xe arc lamp (450 W, Ushio) as a light source according to the literature.[18,22,25] Transmission electron microscopy (TEM) images were obtained using an aberration-corrected TEM (JEM-ARM 200F Neoarm, Jeol) at 200 kV. HAADF-STEM images were collected at 80 kV after stabilization with TEM accessories, using an aberration-corrected NEO ASCOR high-order aberration corrector, according to the literature.[27] AFM measurements were carried out with an aluminum-coated silicon cantilever (ACTA, App Nano) which has a spring constant of 37 N m^{-1}, a resonance frequency of 300 kHz, and an approximate tip radius of 6 nm. Height topographies were recorded, typically capturing a 512 × 512 pixel image over a 5 μm × 5 μm area. Water contact angles were measured with a contact angle goniometer (Phoenix 10, Surface Electro Optics) based on previous work.[28] Optical images were obtained by using an upright fluorescence microscope (BX-51, Olympus) with a complementary metal oxide semiconductor (CMOS) camera (3.4 μm/pixel, 2560 × 1920 pixels).

FC12/(8,6)-SWCNT enrichment

The FC12-assisted SWCNT dispersion and FC12/(8,6)-SWCNT enrichment were obtained according to the literature.[18,22,29–31] Briefly, a mixture of 1 mg HiPco SWCNT, 3 mg FC12 in total 3 mL of varying % of v/v Ch (0, 30, 40, 50, 60, and 70%)/Tol was initially homogenized with a brief bath sonication and subsequent probe sonication for 1 h. After 2 h centrifugation at 30 000*g* of the resulting dispersion, 80% of the supernatant was carefully collected. In this way, FC12/SWCNT dispersions with different Ch/Tol ratios were obtained.

Self-assemblies on device

Tandem alkyl self-assembled monolayer (SAM): The mixtures with varying ratios (0 : 10 to 10 : 0) of chloro(dimethyl)ethylsilane : chloro(dimethyl)octylsilane having total 5 mM anhydrous Tol were utilized to prepare a SAM layer on a bare 285 nm-thick SiO_2/Si substrate. In a parellel effort, inductively coupled plasma (ICP-RIE, IPS-5000, Sntec) was employed to hydrophilize a 285 nm thick SiO_2/Si substrate and remove surface contaminants at 50 W for 5 min in the presence of O_2 flow with 60 sccm. The sandwiched two SiO_2/Si substrates, which faces each other, are placed in the precursor mixture solution for 24 h. The resulting samples were bath-sonicated in Tol for 8 min, followed by ethanol and *n*-hexane washings. *PEGylation on Au electrodes*: Au-patterned substrate was placed into an 3 mM PEG methyl ether thiol in anhyrous Tol. This substrate was kept for 12 h under argon atmosphere and was washed with DI water several times.

Photolithography

AZ5214-E (Merck) was used as photoresist (PR) and was spin-coated on a 285 nm-thick SiO_2/Si substrate at 3000 rpm for 50

s. The sample was soft-baked at 100 °C for 42 s. The photoexposure was conducted by irradiating 365 nm light for 7.3 s corresponding to 84 mJ cm^{-2} with contact mode. The pattern was developed by dipping the sample into AZ300 MIF solution (Merck) for 70 s, followed by DI water cleaning for 60 s. The sample was further dried by spinning the substrate at 4000 rpm for 60 s. 50 nm-thick Au was evaporated by sputtering. The remaining PR was removed by acetone washing.

TFT measurements

Backgate TFT devices were fabricated. The *I–V* characteristics were measured using a semiconductor parameter analyzer (E5270B, Agilent Technologies or Summit 1971B, Cascade Microtech) under ambient conditions. As shown in photographs from Fig. S1A–S1B, probe station (MST4000A, MStech) with Au-coated tungsten probes (M5BG, MStech) were utilized to measure semiconductor characteristics. The transfer characteristics of the SWCNT TFT devices before and after PEGylation were measured under dry conditions without introducing any liquid. *Metal ion detections*: Few μL-sized DI water or metal ion-containing droplet was placed in the channel of TFT device for the measurement.

Results and discussion

Fig. 1A presents a schematic illustration of the TFT device architecture and the proposed mercury-sensing mechanism employing an FC12/monochiral semiconducting SWCNT film as the active TFT layer. The device incorporates multiple self-assembly (SA) motifs formed both on the monochiral *s*-SWCNT network and on the substrate surface, collectively enabling ultrasensitive detection of Hg(II) ions. First, monochiral (8,6)-SWCNTs are isolated *via* a solvent-precipitation sorting process using FC12, synthesized following a previously reported method.[25] During this process, FC12 helically wraps around the (8,6) nanotubes (i), forming a well-defined supramolecular structure.[18,25] This uniform monochiral nanoconstruct allows consistent Hg(II) detection, whereas unsorted SWCNT ensembles typically suffer from reduced sensitivity due to chirality-dependent variations in metal-binding affinity.[23] Second, an optimized ethyl/octyl tandem SAM (ii) is introduced to promote efficient assembly of the FC12/(8,6)-SWCNT random network. Alkyl-chain interdigitation between the SAM and the FC12 side chains enhances film organization and interfacial coupling, thereby improving device sensitivity. Additionally, the gold electrodes are passivated through PEGylation using PEG methyl ether thiol (iii), minimizing nonspecific interactions with analytes. Finally, the self-assembled FC12 helices surrounding the monodisperse (8,6)-SWCNTs enable selective Hg(II) detection through the formation of a flavin–Hg–flavin coordination triad (iv) along the SWCNT sidewalls, as illustrated in the inset of Fig. 1B.[23] This specific coordination interaction produces measurable modulation in the electrical characteristics of the TFT device.

Fig. 1B schematically illustrates the TFT-based detection mechanism of Hg(II) ions in solution. The sensing principle

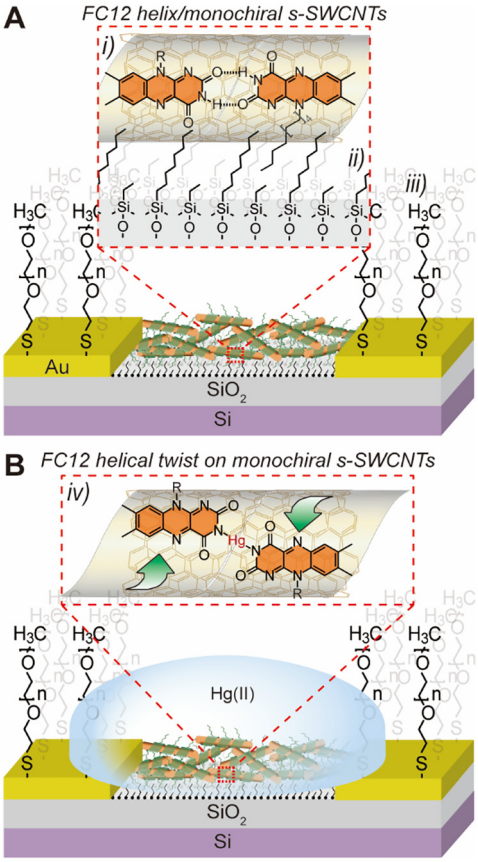

Fig. 1 Schematic for FC12 helix/(8,6)-SWCNT TFT for mercury detection. (A) Schematic for the TFT using FC12 helix/monochiral (8,6)-SWCNT random network film, which is assembled on a tandem alkyl SAM by the interdigitation of dodecyl sidechain of FC12 (inset). Design motifs based on various SAs are denoted as (i), (ii), and (iii). (B) Electrical conductance change of SWCNT network wrapped by FC12 helical twist upon Hg binding by forming flavin–Hg–flavin coordination triad (iv). Metal ions are introduced as aqueous droplet in TFT device.

relies on changes in the electrical conductance of the SWCNT network triggered by the formation of a flavin–Hg–flavin coordination triad. In the absence of Hg(II), adjacent ascending and descending FC12 ribbons are stabilized through quadruple hydrogen bonding, arising from the nearly cofacial alignment of opposing isoalloxazine units.[25] Upon Hg(II) coordination, however, the aligned isoalloxazine moieties undergo slight lateral displacement along the helical axis and bind to the metal ion, as depicted in the inset.[23] A structurally analogous coordination motif (*i.e.*, thymine–Hg–thymine) has been reported within DNA duplexes.[32] The formation of the flavin–Hg–flavin triad induces torsional strain in the monochiral SWCNT mediated by the helical FC12 assembly.[33,34] This structural perturbation alters the charge transport pathway within the nanotube network, resulting in measurable modulation of the device conductance.

The enrichment of FC12/(8,6)-SWCNTs was achieved using a solvent-selective precipitation approach. In a mixed-solvent system composed of a good solvent (Ch) and a poor solvent

(Tol), the preferential interaction between FC12 and (8,6) nanotubes drives selective enrichment, as described in previous reports (see Experimental).[18,25,31] Fig. 2A presents the UV–vis–NIR absorption spectra of the enriched FC12/(8,6)-SWCNTs dispersed in a 60% (v/v) Ch/Tol mixture, alongside unsorted SWCNTs dispersed in toluene. In contrast to the congested spectral features of the unsorted sample—arising from multiple SWCNT chiralities—the enriched FC12/(8,6)-SWCNTs exhibit well-defined absorption peaks corresponding to the first (e_{11}) and second (e_{22}) excitonic transitions at approximately 1202 nm and 737 nm, respectively. These transitions originate from the FC12-wrapped (8,6) nanotubes.

Notably, the observed absorption bands are red-shifted relative to those of sodium dodecyl sulfate (SDS)-wrapped (8,6)-SWCNTs[35] and are consistent with previously reported spectra of flavin-functionalized SWCNTs.[18,25] In addition to the primary e_{11} and e_{22} transitions, satellite features attributed to electron–phonon (*el–ph*) coupling are observed at an energy separation of approximately 200 meV from the main peaks. These sidebands are characteristic of *el–ph* interactions associated with the (8,6) nanotube structure.[18,36]

Photoluminescence excitation (PLE) contour mapping—an effective technique for identifying specific semiconducting SWCNT chiralities[22,25,35,37]—was employed to verify the presence of FC12-assembled (8,6) nanotubes on SAM substrate. The PLE contour map of FC12/(8,6)-SWCNTs deposited on an ethyl/octyl (3 : 7) SAM formed on a quartz substrate (Fig. 2B) shows that the e_{11} and e_{22} transition energies (~1208 nm and ~730 nm, respectively) closely match those observed for the FC12/(8,6)-SWCNT dispersion. This consistency confirms that the supramolecular FC12 assembly surrounding the nanotubes is preserved in the solid state. Furthermore, excitation peaks at 375 nm and 460 nm with emission at 1208 nm originate from energy transfer of FC12 which occurs in close proximity with SWCNTs.[18,38] While these features are strong for FC12/(8,6)-SWCNT films on quartz, they become slightly weaker after the photolithography step, indicating that multiple steps including PR removal further eliminates FC12 on SWCNT.

Moreover, the absence of an excitation feature near 510 nm —characteristic of free flavin molecules[18]—indicates that unbound flavin species are not present in the film. Collectively, these results demonstrate that the helical FC12 wrapping around the (8,6)-SWCNTs remains intact throughout the solid-state assembly process. The resulting FC12/(8,6)-SWCNT thin film was subsequently employed as the active channel material in the TFT devices. Additionally, SWCNT films subjected to photolithographic processing retained similar photoluminescence characteristics (Fig. S2), further confirming the structural integrity of the FC12/(8,6)-SWCNT assembly within the fabricated TFT platform.

TEM was conducted to examine the morphology of the random network formed by FC12-removed (8,6)-SWCNT films. To prepare this sample, a film composed solely of (8,6)-SWCNTs was fabricated by vacuum filtration of the dispersion onto a dissolvable nitrocellulose membrane.[39,40] The membrane-supported film was subsequently treated with excess acetone, which served both to dissolve the nitrocellulose membrane and to remove the FC12 molecules wrapped around the

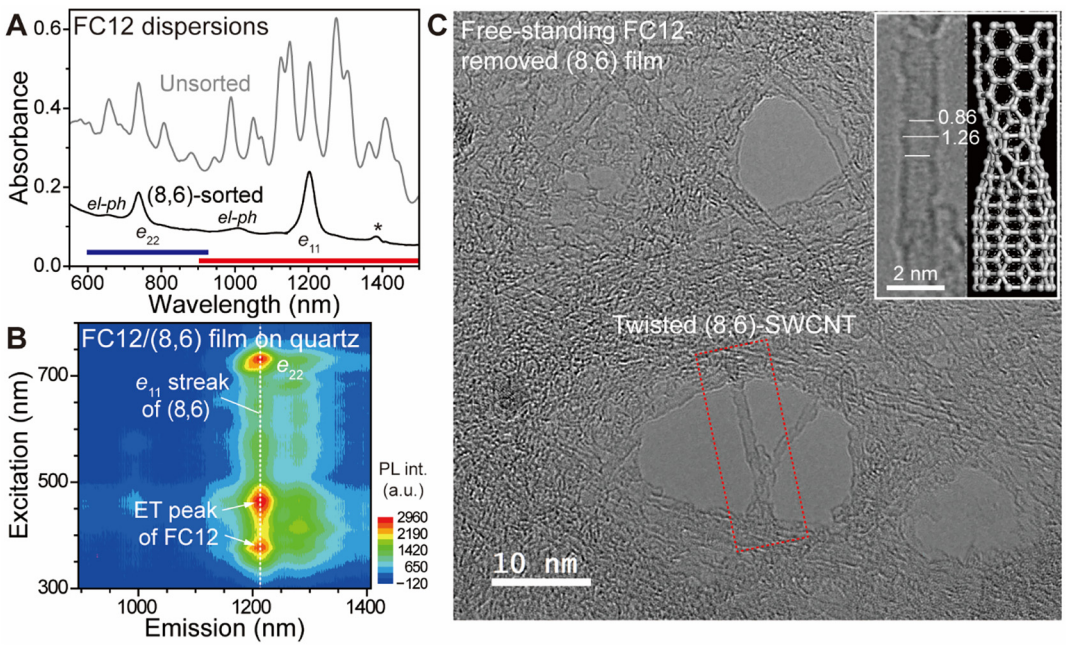

Fig. 2 Characterization of FC12/(8,6)-SWCNTs in solution and film states. (A) UV-Vis-Near IR (NIR) absorption spectra of the separated FC12/(8,6)-SWCNT dispersion in 60% Ch/Tol (black) to the unsorted FC12/SWCNT Tol dipsersion (grey). Peak marked by asterisk originates from residual water. (B) PLE contour map of FC12/(8,6)-SWCNTs assembled on ethyl/octyl 3 : 7 SAM assembled on a quartz substrate. (C) TEM images of FC12-washed (8,6)-SWCNT film on a TEM grid, showing the existence of (8,6)-SWCNT twist (red dashed box) even though FC12 is removed by acetone washing. Inset: zoom-in TEM image of twisted (8,6)-SWCNT without FC12 (left), along with the simulated twisted SWCNT (right).

(8,6)-SWCNTs (see Experimental). TEM image of the film transferred onto a TEM grid (Fig. 2C) reveals that the (8,6)-SWCNTs form twisted strand-like structures. Closer inspection (red dashed box) shows that individual nanotubes exhibit pronounced torsion, characterized by alternating contracted (~0.86 nm) and expanded (~1.26 nm) diameters along their length (inset of Fig. 2C). Given the dense packing within the SWCNT network, this morphology likely originates from the residual torsional strain imparted by the helical FC12 assembly, which appears to persist even after acetone-mediated removal of the flavin molecules. Such spatially regulated diameter modulation indicates characteristics of long-range torsional deformation. This modulation was witnessed in torsion-induced deformation in SWCNTs, reflecting their relatively low torsional rigidity despite high axial stiffness.[41] Furthermore, such deformation can be stabilized by the flavin helical supramolecules, which imposes local torque and couples molecular rearrangement with nanotube deformation.

The surface density of adsorbed FC12/(8,6)-SWCNT networks was regulated using SAMs formed with varying precursor ratios on 285 nm-thick SiO_2/Si substrates. Fig. 3A schematically illustrates the tandem alkyl SAM structure, designed to interdigitate with the dodecyl side chains of the FC12-wrapped (8,6)-SWCNTs. As shown, the precursor ratio of ethyl to octyl silanes governs the intermolecular spacing within the SAM, thereby optimizing the surface environment to accommodate a high density of FC12/(8,6)-SWCNT adsorption. To achieve this tunability, different ratios of chloro(dimethyl)ethylsilane and chloro(dimethyl)octylsilane were employed to fabricate SAMs with controlled surface morphologies. Notably, these silane precursors contain a single chloro functional group and two methyl substituents, structural features that promote defined spacing between adjacent alkyl chains within the monolayer.

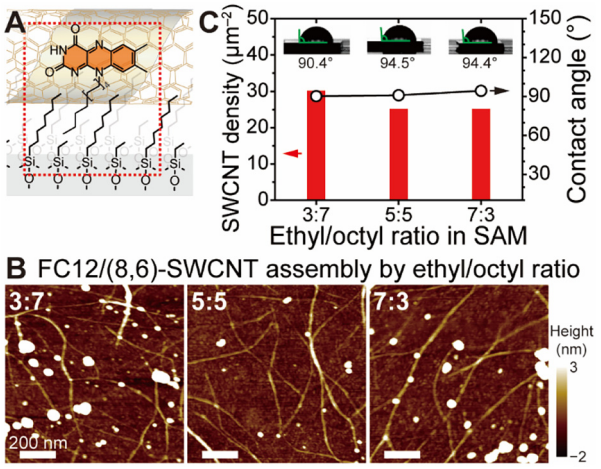

Fig. 3 Maximized FC12/(8,6)-SWCNT random network film assembled on varying tandem alkyl SAMs. (A) Schematic for FC12/(8,6)-SWCNT assembled on an ethyl : octyl tandem SAM. (B) AFM images of the assembled FC12/(8,6)-SWCNT random networks according to ethyl/octyl ratio in SAMs. Scale bar: 200 nm. (C) SWCNT density and water contact angle according to ethyl/octyl ratio of SAM.

Fig. S3A–S3K present AFM height images of the resulting SAMs prepared with ethyl/octyl silane ratios ranging from 0 : 10 to 10 : 0 on 285 nm-thick SiO_2/Si substrates. Fig. S4 shows the corresponding water contact angle measurements for each SAM composition. The contact angle exhibits a saturation trend with increasing ethyl content. Except for a few cases, all measured angles exceed 90°, significantly higher than that of the bare substrate (~73°), indicating enhanced surface hydrophobicity following SAM modification.

Fig. 3B presents AFM images of FC12/(8,6)-SWCNT networks assembled on representative tandem alkyl SAMs with ethyl/octyl precursor ratios of 3 : 7, 5 : 5, and 7 : 3. In all cases, randomly interconnected SWCNT networks are observed. Focusing on nanotube surface density, despite the fact that all corresponding SAMs exhibit water contact angles greater than 90° (Fig. 3C), the highest SWCNT density (~30 tubes per μm^2) is obtained for the 3 : 7 SAM. In comparison, the 5 : 5 and 7 : 3 SAMs show lower densities of approximately 25 tubes per μm^2. It is well established that SWCNT adsorption can be modulated by the structural characteristics of underlying SAMs.[28,42] These results suggest that the 3 : 7 tandem alkyl SAM provides optimal intermolecular spacing between octyl chains, effectively accommodating the dodecyl side chains of FC12-wrapped (8,6)-SWCNTs through van der Waals (vdW)-driven alkyl interdigitation.

Next, the mercury-sensing performance of TFTs based on FC12/(8,6)-SWCNT random networks was evaluated. Fig. 4A schematically illustrates the proposed Hg(II) sensing mechanism in solution, highlighting the formation of a flavin–Hg–flavin coordination triad along the SWCNT sidewalls. The numbered annotations (1, 2, and 3) indicate key contributing factors: (i) PEGylation for minimizing nonspecific interactions, (ii) intrinsic transistor characteristics, and (iii) mercury ion sensitivity, which will be discussed in detail below. For device fabrication, conventional photolithography was employed (see Experimental). The FC12/(8,6)-SWCNT film assembled on a 3 : 7 ethyl/octyl SAM atop a 285 nm-thick SiO_2/Si substrate was patterned using a metal mask, followed by deposition of Au electrodes *via* sputtering. Fig. 4B shows an optical image of the fabricated TFT device, featuring a channel length of 20 μm and a channel width of 231 μm. The SWCNT random network is clearly visible within the defined channel region.

PEGylation plays a critical role in stabilizing device operation under droplet-based sensing conditions having multiple interface. First, PEG forms a hydrophilic and electrically insulating layer on the device surface which suppresses the formation of parasitic ionic conduction pathways in the presence of a liquid droplet and influence device current and stability.[43,44] Next, PEG reduces the adsorption of charged ionic species near the nanotube channel and electrode regions, thereby minimizing unintended electrostatic gating effects in which PEG enables more reproducible electrical signals.[45,46] As a result of these combined effects, the PEG-treated device exhibits reduced leakage current, improved baseline stability, and enhanced electrical performance under sensing conditions.

Fig. 4C compares the current–voltage (I–V) characteristics of the FC12/(8,6)-SWCNT TFT devices measured in the presence

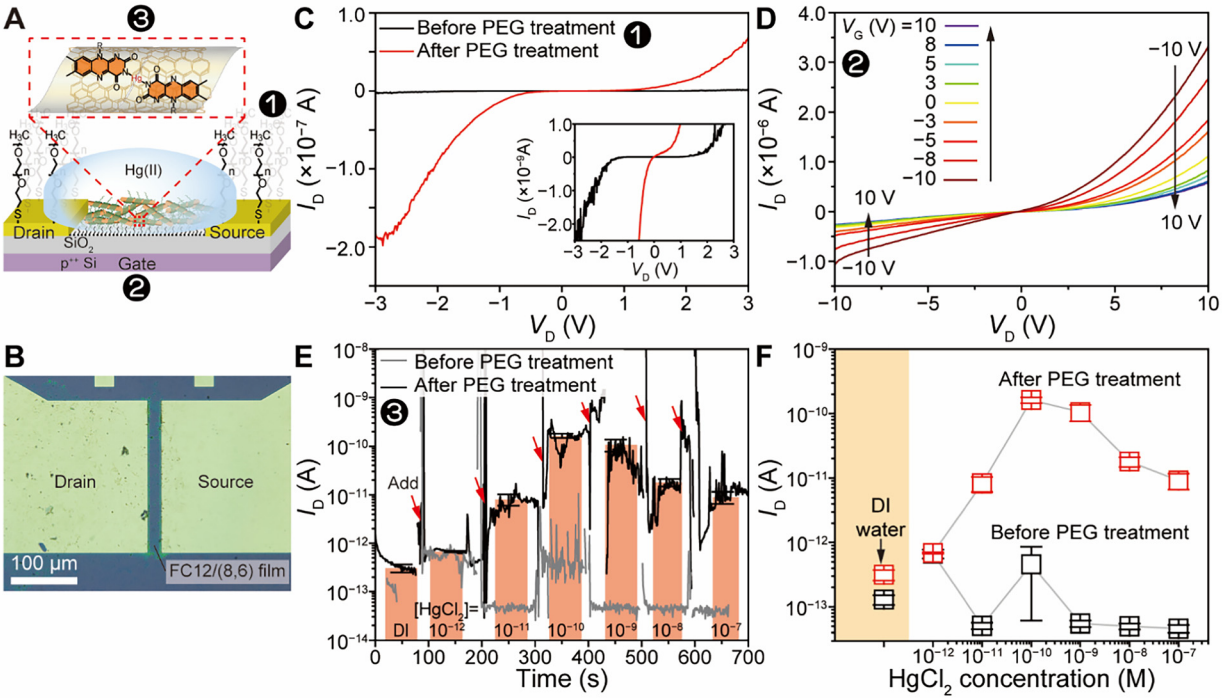

Fig. 4 TFT performance and Hg-sensing characteristics of FC12/(8,6)-SWCNT devices before and after PEGylation on Au electrodes. (A) Schematic for PEGylated TFT device based on FC12/(8,6)-SWCNT random network film. Numbers indicates the investigating parameters. (B) Optical image of the fabrication TFT device. The channel length and width are 20 μm and 231 μm, respectively. (C) Effect of PEGylation on Au electrodes for I_D–V_D characteristics of FC12/(8,6)-SWCNT TFT device, with V_G = 0 V. Inset: magnified view of low-current regime. (D) I_D–V_D characteristics of the PEGylated TFT device without $HgCl_2$ addition according to V_G. (E) I_D measurement of TFT device according to PEGylation and Hg(II) concentrations. Conditions: V_D = 0.1 V, V_G = 0 V. The flat signal parts right after the spike originating from the sample addition was set as I_D. Different Hg ion concentrations were added to the existing droplet on TFT device which made current signal spikes as indicated by red arrow. (F) I_D levels of the device with or without PEGylation.

and absence of PEG treatment on the Au electrodes. Electrical sensing measurements were conducted by applying deionized (DI) water onto the channel region containing the SWCNT random network bridging the Au electrodes. In the untreated device, the drain current I_D exhibits minimal response over a drain voltage V_D sweep from −3 to 3 V. In contrast, the PEGylated device displays clear semiconducting behavior, with an exponential increase in current reaching approximately 10^{-7} A. In the low-bias region (−0.2 to 0.2 V), the conductance (G) of the PEG-treated TFT is approximately 8.3 × 10^{-10} S, which is nearly two orders of magnitude higher than that of the untreated device (~10^{-12} S) (see Note S1 for detailed analysis). These findings demonstrate that PEGylation effectively suppresses undesired current leakage at the liquid–electrode interface. Notably, the magnified I–V curves shown in the inset reveal that the untreated device still exhibits semiconducting characteristics, albeit with a higher turn-on voltage and significantly lower current levels. This comparison further highlights the critical role of PEG modification in minimizing nonspecific interfacial interactions and improving device performance.[47] Similarly, the transfer characteristics were measured (Fig. S5). Both devices exhibit typical p-type SWCNT TFT behavior, showing I_D increase at negative gate voltages.[48] The threshold voltage remains nearly unchanged after PEGylation, indicating negligible doping effects. The overall current level shows only minor variation within one order of magnitude, suggesting that the intrinsic transport properties of the SWCNT channel are preserved.

Next, the gate voltage (V_G) dependence of I–V curves was investigated. As shown in Fig. 4D, increasing V_G results in decreased I_D at both sides of V_D, indicating p-type semiconductor behavior which is in line with the report.[24,49] In addition, greater reduction for increased V_G was witnessed as well. Fig. 4E shows the I_D responses upon the additions of increasing $HgCl_2$ from 1 pM to 100 nM, while maintaining a constant V_D at −0.1 V. The addition of mercury ion results in spike-like increase, followed by rapid exponential decay to equilibrium I_D in which its average values are utilized for I_D. Hg^{2+} ions are known to form a coordination complex with flavin in a 1 : 1 or 2 : 1 ratios with or without SWCNT.[23] Interestingly, the addition of Hg^{2+} ions in the device enable to detect as small as 1 pM and linearly increase I_D signal up to 100 pM, and shows decreased I_D at later concentration stage. The Hg^{2+} sensing mechanism in this system is governed by the formation of multimodal complexes on the SWCNT surface, which is inherently irreversible.[23] As a result, successive Hg^{2+} exposure leads to a cumulative (or memory) effect, where previously adsorbed species continue to influence the electrical

response, as commonly observed in CNT-based sensors.[50,51] To decouple this contribution, the net I_D change at each concentration step was extracted by subtracting the previous current level (Fig. S6). Notably, even after removing the cumulative effect, the device maintains a clear concentration-dependent response, confirming that the sensing behavior is robust.

Fig. 4F shows the average I_D after its equilibrium of the addition of each Hg^{2+} concentration. $\langle I_D \rangle$ linearly increases as increasing Hg^{2+} concentration in the range of 1 pM to 100 pM. The performance of TFT device surpass not only the typical spectroscopic micromolar detection limit based on flavin–Hg–flavin triad[23] but also the ppb level exposure limit (1 ppb = ~50 nM) for toxic heavy metal ions. Flavin-wrapped SWCNTs form stable helical assemblies through π–π interactions and intermolecular hydrogen bonding.[23] Hg^{2+} ions can coordinate with flavin in both 1 : 1 and 2 : 1 binding modes, forming Hg-bridged structures that induce conformational changes in the helical assembly on the SWCNT surface.[23] These structural variations modify intermolecular interactions with the SWCNT, which is known to influence its electronic structure and conductance.[41] Consequently, initial Hg^{2+} binding enhances charge transport *via* charge transfer or dipole modulation, whereas higher concentrations lead to structural disorder and increased scattering, resulting in reduced current. In addition, the device without PEG treatment does not result in systematic response, presumably forming Au–Hg amalgam with Au electrodes.

We attribute this behavior to variations in the electrical conductance of SWCNTs induced by torsional deformation associated with the FC12 helical wrapping. The flavin helix exhibits strong binding affinity toward (8,6)-SWCNTs due to their favorable diameter matching.[22] Upon introduction of Hg^{2+} ions, the formation of a flavin–Hg–flavin coordination triad along the nanotube sidewall preferentially occurs.[23] Because the flavin helix serves as the primary stabilizing motif for SWCNT dispersion, Hg^{2+} coordination alters the supramolecular organization of the helix and consequently modulates the degree of nanotube twisting observed (Fig. 2C). The observed decrease in conductance of the FC12/(8,6)-SWCNT network is likely associated with partial slippage or structural rearrangement of the flavin–Hg–flavin helices along an overtwisted SWCNT backbone. Such conformational changes can perturb π–π interactions and charge transport pathways within the nanotube. As a result, modulation of the flavin assembly and the accompanying torsional strain in the SWCNT lead to measurable changes in I_D through conductance variation.

It is noteworthy that flavin assembly on SWCNT remains mobile, as evidenced by the evolution of binding affinity and wrapping configuration upon aging of the flavin–SWCNT assembly.[52,53] Furthermore, the supramolecular assembly motif of flavin varies depending on the underlying SWCNT chirality, indicating that the interaction and local registry are not fixed but chirality-dependent.[30,53–55] In addition, the incorporation of Hg^{2+} into the flavin–SWCNT assembly has been previously reported, demonstrating that external species can interact with and perturb the supramolecular coating.[23] Taken together, these observations indicate that the flavin layer is not rigidly immobilized but can undergo structural rearrangement depending on molecular affinity, environmental conditions, and nanotube chirality.[52]

Another question is whether the observed sensing response is selective toward mercury ions over other metal species. To address this, control experiments were conducted in which I_D of the FC12/(8,6)-SWCNT TFT was measured while incrementally increasing the concentrations of $NiCl_2$ and $FeCl_3$ under conditions identical to those used for Hg^{2+} detection. Ni^{2+} and Fe^{3+} were selected as representative interfering ions due to their common presence in environmental and biological systems and sensor behaviors originating from non-specific binding. The resulting I_D responses are presented in Fig. 5A. As the concentration of Ni^{2+} or Fe^{3+} increased, I_D exhibited irregular fluctuations, showing neither a consistent increase nor decrease with concentration. Fig. 5B summarizes the relationship between metal ion concentration and I_D, clearly demonstrating the absence of any systematic dependence for these ions. Notably, previous dispersion studies have shown that only mercury ions maintain stable FC12/(8,6)-SWCNT dispersions through specific coordination interactions, whereas other divalent or trivalent metal ions tend to induce aggregation and precipitation.[23] This distinct behavior further supports the selective recognition of Hg^{2+} in the present TFT sensing platform. Nevertheless, we acknowledge that a broader investigation including additional metal ions (*e.g.*, Cu^{2+}, Pb^{2+}, Zn^{2+}, and Cd^{2+}) would provide a more comprehensive assessment of selectivity. Such studies will be the focus of future work to further validate the sensor performance in complex matrices.

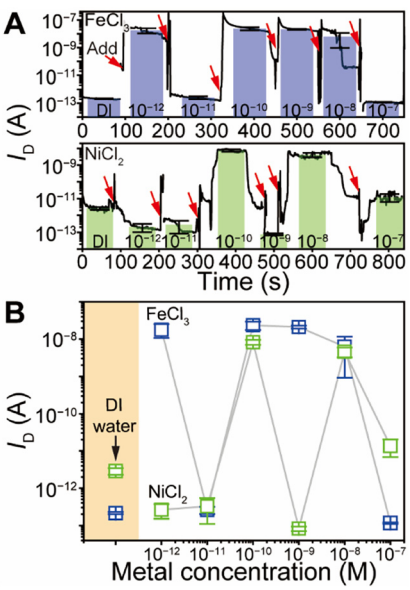

Fig. 5 Selectivity of FC12/(8,6)-SWCNT TFT device for other metal ions. (A) Concentration-dependent I_D response plot for increasing metal ion additions (*i.e.*, $FeCl_3$ and $NiCl_2$) with certain time interval. V_D = 0.1 V. (B) Average I_D trend for each metal concentration.

Such sensing behavior is difficult to achieve using unsorted SWCNT networks. This is because unsorted SWCNTs contain metallic nanotubes, which introduce conductive pathways that cannot be effectively modulated by the gate field due to the absence of a bandgap, resulting in degraded transistor performance and reduced gate controllability.[48] As a result, current changes induced by molecular binding would be less pronounced.

Conclusions

In summary, we demonstrate that a monochiral SWCNT-based TFT device incorporating a molecular recognition motif enables ultrasensitive detection of mercury ions down to 1 pM —representing a six-order-of-magnitude improvement compared with spectroscopic methods employing a similar recognition chemistry. The enhanced sensing performance arises from two key strategies: the isolation of monochiral semiconducting (8,6)-SWCNTs to ensure uniform electronic characteristics, and the maximized assembly of FC12/(8,6)-SWCNT networks on a tailored tandem alkyl SAM within the TFT architecture. Selective mercury detection is achieved through the construction of a specific molecular recognition site—the flavin–Hg–flavin coordination triad—formed along the SWCNT sidewalls, which imparts high Hg^{2+} sensitivity. In addition, PEGylation of the Au electrodes plays a crucial role by minimizing nonspecific adsorption and interfacial interference, thereby improving sensing reliability. These label-free TFT devices enable highly sensitive mercury ion detection over a concentration range of 1–100 pM. More broadly, the integration of molecular recognition motifs with monochiral semiconducting SWCNTs presents a promising platform for early-stage detection of environmental contaminants and disease-related biomarkers in aqueous systems.

Author contributions

D. H. Kim performed sample preparation, measurements, and characterization. S. Hwang performed monochiral enrichment of SWCNT. Y. Kang assisted drawings of figures. S.-Y. Ju and D. H. Kim conceived idea and co-wrote manuscript. All images/artwork/photos that appear in the manuscript and SI file, including those in the TOC graphic, were created by the authors of this manuscript.

Conflicts of interest

There are no conflicts to declare.

Data availability

The data supporting this article have been included as part of the supplementary information (SI). Supplementary information is available. See DOI: https://doi.org/10.1039/d6nr00764c.

Acknowledgements

This research was supported financially by YU-KRISS (KRISS-GP2026-0012-GONG7), and in part by the Basic Science Research Program (RS-2025-23523854, RS-2026-25471952) through the National Research Foundation of Korea (NRF) funded by the Ministry of Education, Science, and Technology.

References

1 T. W. Clarkson, L. Magos and M. J. Gary, *N. Engl. J. Med.*, 2003, **349**, 1731–1737.
2 R. Von Burg, *J. Appl. Toxicol.*, 1995, **15**, 483–493.
3 V. Schroeder, S. Savagatrup, M. He, S. Lin and T. M. Swager, *Chem. Rev.*, 2019, **119**, 599–663.
4 M. B. Gumpu, S. Sethuraman, U. M. Krishnan and J. B. B. Rayappan, *Sens. Actuators, B*, 2015, **213**, 515–533.
5 T. Zhang, Z. Cheng, Y. Wang, Z. Li, C. Wang, Y. Li and Y. Fang, *Nano Lett.*, 2010, **10**, 4738–4741.
6 J. Tu, Y. Gan, T. Liang, Q. Hu, Q. Wang, T. Ren, Q. Sun, H. Wan and P. Wang, *Front. Chem.*, 2018, **6**, 333.
7 H. Wang, Y. Liu and G. Liu, *Nanomaterials*, 2018, **8**, 258.
8 H. Wang, Y. Liu, J. Wang, B. Xiong and X. Hou, *Mikrochim. Acta*, 2020, **187**, 207.
9 Y. Jin, A. Gao, Q. Jin, T. Li, Y. Wang and J. Zhao, *Nanotechnology*, 2018, **29**, 135501.
10 A. Nigam, N. Goel, T. N. Bhat, M. T. Rahman, S. B. Dolmanan, Q. Qiao, S. Tripathy and M. Kumar, *Sens. Actuators, B*, 2020, **309**, 127832.
11 S. Jiang, R. Cheng, R. Ng, Y. Huang and X. Duan, *Nano Res.*, 2015, **8**, 257–262.
12 H. Wang, Y. Yin and L. Gang, *Electroanalysis*, 2019, **31**, 1174–1181.
13 X. Huang, J. Li, Q. Zhang, S. Chen, W. Xu, J. Wu, W. Niu, J. Xue and C. Li, *J. Electroanal. Chem.*, 2018, **816**, 75–82.
14 H. Wang, Y. Liu and G. Liu, *Mikrochim. Acta*, 2018, **185**, 142.
15 F. Torricelli, D. Z. Adrahtas, Z. Bao, M. Berggren, F. Biscarini, A. Bonfiglio, *et al.*, *Nat. Rev. Methods Primers*, 2021, **1**, 66.
16 R. Porrazzo, A. Luzio, S. Bellani, G. E. Bonacchini, Y. Y. Noh, Y. H. Kim, G. Lanzani, M. R. Antognazza and M. Caironi, *ACS Omega*, 2017, **2**, 1–10.
17 S. Hwang, S. Son, M. Park, I.-S. Choi and S.-Y. Ju, *Small Sci.*, 2024, **4**, 2400011.
18 S. Hwang, I.-S. Choi and S.-Y. Ju, *J. Phys. Chem. Lett.*, 2025, **16**, 3438–3446.
19 S. Falina, M. Syamsul, N. A. Rhaffor, S. S. Hamid, K. A. M. Zain, A. A. Manaf and H. Kawarada, *Biosensors*, 2021, **11**, 478.
20 G. D. Kong, S. E. Byeon, S. Park, H. Song, S. Y. Kim and H. J. Yoon, *Adv. Electron. Mater.*, 2020, **6**, 1901157.
21 S.-Y. Ju and F. Papadimitrakopoulos, *J. Am. Chem. Soc.*, 2008, **130**, 655–664.
22 S.-Y. Ju, J. Doll, I. Sharma and F. Papadimitrakopoulos, *Nat. Nanotechnol.*, 2008, **3**, 356–362.

23 M. Park, K.-I. Hong, S.-M. Jin, E. Lee, W.-D. Jang and S.-Y. Ju, *ACS Appl. Mater. Interfaces*, 2019, **11**, 8400–8411.
24 M. Park, S. Kim, H. Kwon, S. Hong, S. Im and S.-Y. Ju, *ACS Appl. Mater. Interfaces*, 2016, **8**, 23270–23280.
25 S.-Y. Ju, W. P. Kopcha and F. Papadimitrakopoulos, *Science*, 2009, **323**, 1319–1323.
26 P. Nikolaev, M. J. Bronikowski, R. K. Bradley, F. Rohmund, D. T. Colbert, K. A. Smith and R. E. Smalley, *Chem. Phys. Lett.*, 1999, **313**, 91–97.
27 D. H. Kim, J. Seo, Y. Kang, B. Lee and S.-Y. Ju, *Nanoscale*, 2025, **17**, 14887–14896.
28 J. Park, Y. R. Han, M. Park, C.-H. Jun and S.-Y. Ju, *Carbon*, 2020, **161**, 599–611.
29 I.-S. Choi, M. Park, E. Koo and S.-Y. Ju, *Carbon*, 2021, **184**, 346–356.
30 J. Sim, H. Oh, E. Koo and S.-Y. Ju, *Phys. Chem. Chem. Phys.*, 2013, **15**, 19169–19179.
31 K. Ozono, M. Fukuzawa, F. Toshimitsu, T. Shiraki, T. Fujigaya and N. Nakashima, *Bull. Chem. Soc. Jpn.*, 2018, **91**, 1646–1651.
32 J.-S. Lee, M. S. Han and C. A. Mirkin, *Angew. Chem., Int. Ed.*, 2007, **46**, 4093–4096.
33 S.-Y. Ju, D. C. Abanulo, C. A. Badalucco, J. A. Gascón and F. Papadimitrakopoulos, *J. Am. Chem. Soc.*, 2012, **134**, 13196–13199.
34 J. Sim, S. Kim, M. Jang, M. Park, H. Oh and S.-Y. Ju, *Langmuir*, 2017, **33**, 11000–11009.
35 M. J. O'Connell, S. M. Bachilo, C. B. Huffman, V. C. Moore, M. S. Strano, E. H. Haroz, *et al.*, *Science*, 2002, **297**, 593–596.
36 Y. Murakami, B. Lu, S. Kazaoui, N. Minami, T. Okubo and S. Maruyama, *Phys. Rev. B: Condens. Matter Mater. Phys.*, 2009, **79**, 195407.
37 S. M. Bachilo, M. S. Strano, C. Kittrell, R. H. Hauge, R. E. Smalley and R. B. Weisman, *Science*, 2002, **298**, 2361–2366.
38 A. Nish, J.-Y. Hwang, J. Doig and R. J. Nicholas, *Nanotechnology*, 2008, **19**, 095603.
39 M. Park, S. Hwang, T. Nakae, H. Sakaguchi and S.-Y. Ju, *ACS Appl. Mater. Interfaces*, 2025, **17**, 18482–18492.
40 M. Park and S.-Y. Ju, *Bull. Korean Chem. Soc.*, 2022, **43**, 196–200.
41 A. R. Hall, M. R. Falvo, R. Superfine and S. Washburn, *Nat. Nanotechnol.*, 2007, **2**, 413–416.
42 X. Liu, C. Chen, P. Sharma, L. Zhang, Y. Wang, N. Hu, *et al.*, *Phys. E*, 2015, **74**, 451–456.
43 B. Shkodra, M. Petrelli, M. A. C. Angeli, D. Garoli, N. Nakatsuka, P. Lugli and L. Petti, *Appl. Phys. Lett.*, 2021, **8**, 041325.
44 T. Ozel, A. Gaur, J. A. Rogers and M. Shim, *Nano Lett.*, 2005, **5**, 905–911.
45 M. Krüger, M. R. Buitelaar, T. Nussbaumer, C. Schönenberger and L. Forró, *Appl. Phys. Lett.*, 2001, **78**, 1291–1293.
46 A. W. Bushmaker, V. Oklejas, D. Walker, A. R. Hopkins, J. Chen and S. B. Cronin, *Nat. Commun.*, 2016, **7**, 10475.
47 R. J. Chen, H. C. Choi, S. Bangsaruntip, E. Yenilmez, X. Tang, Q. Wang, Y.-L. Chang and H. Dai, *J. Am. Chem. Soc.*, 2004, **126**, 1563–1568.
48 S. Heinze, J. Tersoff, R. Martel, V. Derycke, J. Appenzeller and P. Avouris, *Phys. Rev. Lett.*, 2002, **89**, 106801.
49 E. S. Snow, P. M. Campbell, M. G. Ancona and J. P. Novak, *Appl. Phys. Lett.*, 2005, **86**, 033105.
50 J. Kong, N. R. Franklin, C. Zhou, M. G. Chapline, S. Peng, K. Cho and H. Dai, *Science*, 2000, **287**, 622–625.
51 L. Zhang, T. Li, B. Li, J. Li and E. Wang, *Chem. Commun.*, 2010, **46**, 1476–1478.
52 F. Ke, J. Chen, R. Wu and Y. Chen, *Nanotechnology*, 2020, **31**, 255708.
53 M. Park, J. Park, J. Lee and S.-Y. Ju, *Carbon*, 2018, **139**, 427–436.
54 R. Sharifi, M. Samaraweera, J. A. Gascón and F. Papadimitrakopoulos, *J. Am. Chem. Soc.*, 2014, **136**, 7452–7463.
55 H. Oh, J. Sim and S.-Y. Ju, *Langmuir*, 2013, **29**, 11154–11162.